inorganics

MDPI

Article

GaAs Quantum Dot Confined with a Woods–Saxon Potential: Role of Structural Parameters on Binding Energy and Optical Absorption

Hassen Dakhlaoui [1], Walid Belhadj [2,*], Haykel Elabidi [2], Fatih Ungan [3] and Bryan M. Wong [4,*]

[1] Nanomaterials Technology Unit, Basic and Applied Scientific Research Center (BASRC), Physics Department, College of Science of Dammam, Imam Abdulrahman Bin Faisal University, P.O. Box 1982, Dammam 31441, Saudi Arabia

[2] Physics Department, Faculty of Applied Science, Umm AL-Qura University, P.O. Box 715, Makkah 21955, Saudi Arabia; haelabidi@uqu.edu.sa

[3] Department of Physics, Faculty of Science, Sivas Cumhuriyet University, 58140 Sivas, Turkey

[4] Materials Science & Engineering Program, Department of Chemistry, and Department of Physics & Astronomy, University of California-Riverside, Riverside, CA 92521, USA

* Correspondence: wbbelhadj@uqu.edu.sa (W.B.); bryan.wong@ucr.edu (B.M.W.)

Abstract: We present the first detailed study of optical absorption coefficients (OACs) in a GaAs quantum dot confined with a Woods–Saxon potential containing a hydrogenic impurity at its center. We use a finite difference method to solve the Schrödinger equation within the framework of the effective mass approximation. First, we compute energy levels and probability densities for different parameters governing the confining potential. We then calculate dipole matrix elements and energy differences, $E_{1p} - E_{1s}$, and discuss their role with respect to the OACs. Our findings demonstrate the important role of these parameters in tuning the OAC to enable blue or red shifts and alter its amplitude. Our simulations provide a guided path to fabricating new optoelectronic devices by adjusting the confining potential shape.

Keywords: optical absorption coefficient; spherical quantum dots; Schrödinger equation; hydrogenic impurity; Woods–Saxon potential

check for updates

Citation: Dakhlaoui, H.; Belhadj, W.; Elabidi, H.; Ungan, F.; Wong, B.M. GaAs Quantum Dot Confined with a Woods–Saxon Potential: Role of Structural Parameters on Binding Energy and Optical Absorption. *Inorganics* **2023**, *11*, 401. https://doi.org/10.3390/inorganics11100401

Academic Editor: Sake Wang, Minglei Sun and Nguyen Tuan Hung

Received: 18 September 2023
Revised: 7 October 2023
Accepted: 10 October 2023
Published: 13 October 2023

1. Introduction

The tunability of energy levels in low dimensional systems such as quantum wells (QWs), quantum wires (QWRs), and quantum dots (QDs) enable a multitude of optoelectronic devices, such as quantum cascade lasers, optical modulators, optical switches, and infrared photodetectors [1–4]. In addition, QDs are used in the creation of universal memory elements due to their spatial distribution of free carriers that are confined in three dimensions [5–8]. Generally, the position of different energy levels is determined via the geometrical shape of the confining potential of the quantum structure, such as square, parabolic, semi-parabolic, Gaussian, Razavy, Konwent, and Manning shapes [9–14]. QDs are of particular interest in optical applications due to their luminescence, potential to emit different frequencies with intense efficacies, high extinction, and prolonged lifetimes [15–17]. For these reasons, QDs are used in other technological applications such as light-emitting diodes (LEDs), electronic transistors, medical laser imaging, biosensors, quantum cascade lasers, and quantum computing architectures [18–25].

QDs generally show larger energetic separations between different levels compared to QWs and QWRs due to the three-dimensional confinement of carriers. They also give more intense density of states (DOS) than other quantum systems, which enables them to be used in amplifier applications. In addition to the geometry and shape of the confining potential, the incorporation of a hydrogenic impurity in QDs can modulate electronic and optical absorption coefficients (OACs) due to the electrostatic attraction between the free electrons and the impurity [26–32]. Previous work on OACs in QDs has focused on both theoretical and experimental studies [33–36]. For instance, Schrey et al. studied the optical absorption of quantum dots in photodetectors and analyzed the effect of QD size on their minibands [37]. Bahar et al. calculated OACs of a QD with a hydrogenic impurity in a Mathieu potential and found that the OAC and refractive index were affected by hydrostatic pressure and temperature variations [38]. Batra and coauthors examined structural parameters and the optical response of a QD with a tunable Kratzer confining potential [39]. Bassani et al. treated the effects of donor and acceptor impurities on OACs in a spherical QD [40]. The process of intraband and interband absorption in an InGaAs/GaAs QD was studied by Narvaez et al. [41], and the effects of size and distance separating QDs were evaluated by Stoleru et al. [42] The oscillator strengths between lower energy state transitions in a spherical QD with a hydrogenic impurity were calculated by Yilmaz et al. [43]. Kirak and coauthors evaluated the effect of an applied electric field on the OAC in a spherical QD with a parabolic potential under the influence of a hydrogenic impurity [44]. Fakkahi et al. studied OACs and oscillator strengths in multilayer spherical QDs under the influence of a radial electric field and hydrogenic impurities. Other works on OACs in multiple spherical QDs are also discussed in references [45–48].

Motivated by these studies, we investigate the electronic and optical properties of electrons confined in a GaAs quantum dot with a radial confinement described by the Woods–Saxon confining potential. The functional form of this potential was first proposed to describe and interpret interactive forces in the nuclear shell model [49]. Furthermore, this confining potential describes a smooth interface structure and gives an accurate description of aluminum diffusion from the AlGaAs barrier towards the GaAs quantum well. Our study commences with a calculation of the 1s and 1p energy levels and their probability densities as a function of structural parameters in the Woods–Saxon potential. We then analyze the dipole matrix elements (DMEs) and OACs as the parameters of the Woods–Saxon potential are varied in the presence of a hydrogenic impurity. Further details and approximations of our theoretical model are given in Section 2. In Section 3, our findings and the resulting physical observables are discussed. Finally, Section 4 summarizes our results.

2. Theoretical Modeling

2.1. Woods–Saxon Potential Form

We begin this section by discussing the confining potential and its structural parameters. These parameters alter the geometrical form of the potential and affect the position of different energy levels. When the confining potential is spherically symmetric, the carrier's motion is quantized and described by angular and magnetic quantum numbers, with the associated wave functions being expressed as a function of the well-known spherical harmonics. The form of the radial electronic wavefunctions is mainly determined by the geometrical shape of the confining potential. Since the energy separation, $E_{1p} - E_{1s}$, between the initial and final states, plays a major role in the OAC expression, we examine its dependence on QD size, the structural parameters of the confining potential, or both.

We first examine the radial Woods–Saxon potential, which is given by [45]

$$V_{\rm ws}(r) = \frac{V_0}{1+\exp[(R_0-r)/\gamma]} + \frac{V_0}{1+\exp[(R_0+r)/\gamma]}. \tag{1}$$

V_0 is the height of the Woods–Saxon potential and $R_0 = R/2$, where R denotes the QD radius, and γ is a parameter characterizing the slope between the well and barrier regions.

Figure 1 depicts a schematic of the quantum dot, which consists of a GaAs core with radius $R = 25$ nm surrounded by an AlGaAs barrier. This latter has an external radius of $R_{\rm ext} = 2R$.

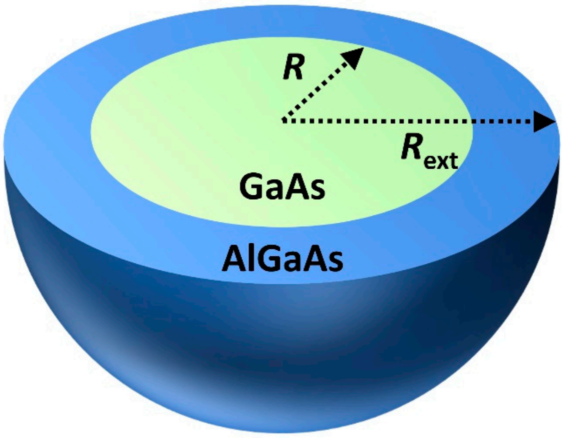

Figure 1. Schematic structure of spherical GaAs quantum dot surrounded by an AlGaAs barrier.

Before studying the optical properties of our structure, we plot the geometrical dependence of the Woods–Saxon potential on the parameter γ in Figure 2a–d. The radius of the QD is $R = 25$ nm. For $\gamma = 5$ Å, the Woods–Saxon potential resembles a square quantum well since it takes a flat form between 0 and 5 Å. However, when γ increases, the bottom of the potential becomes more parabolic. Furthermore, the top of the well becomes more curved as γ increases. For instance, the potential reaches 1500 meV at $r = 10$ nm for $\gamma = 5$ Å (Figure 2a); however, it reaches this value at $r = 15$ nm for $\gamma = 20$ Å in Figure 2d. Increasing the parameter γ influences the distribution of the confined energy levels and consequently affects the energy separation and OAC.

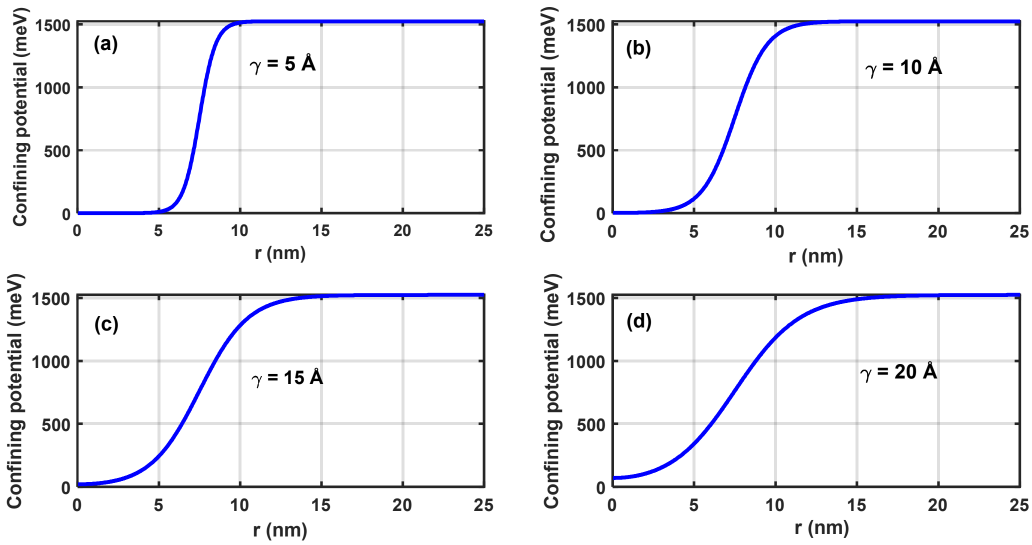

Figure 2. Woods–Saxon potential profile for (**a**) $\gamma = 5$ Å, (**b**) $\gamma = 10$ Å, (**c**) $\gamma = 15$ Å, and (**d**) $\gamma = 20$ Å. The radius of the QD is fixed at $R = 25$ nm with $R_0 = R/2$, $V_0 = 0.228$ eV, and $R_{\text{ext}} = 2R$.

2.2. Calculation of Electronic and Optical Properties

An electron in a spherical QD with a hydrogenic impurity within the effective mass approximation can be completely described by solving the radial Schrödinger equation [10,43,44]:

$$\left[-\frac{\hbar^2}{2}\vec{\nabla}_r\left(\frac{1}{m^*(r)}\vec{\nabla}_r\right)+\frac{\ell(\ell+1)\hbar^2}{2m^*(r)\,r^2}-\frac{Z\,e^2}{\varepsilon\,r}+V_{\text{ws}}(r)\right]R_{n\ell}(r)=E_{n\ell}\,R_{n\ell}(r), \tag{2}$$

where $m^*(r)$ is the position-dependent mass of the electron, $\hbar$ represents the reduced Planck constant, ε is the dielectric constant, and ℓ is the angular quantum number. Furthermore, $R_{n\ell}(r)$ and $E_{n\ell}$ are the radial wavefunction and energy eigenvalue, respectively.

The first term in Equation (2) represents the kinetic energy, whereas the second term containing $\ell(\ell+1)$ denotes the centrifugal contribution of the potential due to the spherical symmetry of the Woods–Saxon potential. The third term represents the electron-impurity attraction. The two cases, $Z = 0$ and $Z = 1$, correspond to the absence and presence of the hydrogenic impurity, respectively. $V_{\text{ws}}(r)$ represents the Woods–Saxon potential which is a radial confinement term. To compute $E_{n\ell}$ and $R_{n\ell}(r)$, we discretized Equation (2) using the finite difference method and transformed it into a linear eigenvalue equation of the form $AX = \lambda X$, where A is a tridiagonal matrix, X represents $R_{n\ell}(r)$, and λ denotes $E_{n\ell}$. The 1D discretization of the radial Schrödinger equation was carried out with a finite difference method (FDM). Thus, Equation (2) takes the linear form:

$$\begin{aligned} R_{n\ell}(j+1)\left[-\frac{\hbar^2}{2m^* r_j(\Delta r)} - \frac{\hbar^2}{2m^*(\Delta r)^2}\right] + R_{n\ell}(j)\left[\frac{\hbar^2}{m^*(\Delta r)^2} + \frac{\ell(\ell+1)}{m^*\left(r_j.\Delta r\right)^2} + \quad V_{WS}(j)\right] \\ +R_{n\ell}(j-1)\left[\frac{\hbar^2}{2m^* r_j(\Delta r)} - \frac{\hbar^2}{2m^*(\Delta r)^2}\right] = E_{n\ell} R_{n\ell}(j), \end{aligned} \tag{3}$$

where $r_j = j\Delta r\ (j = 1, \ldots, N)$ and $\Delta r = \frac{R}{N}$ is the mesh discretization. Equation (3) is of the form $Hx = \lambda x$, where λ is the energy $E_{n\ell}$, x is the radial wavefunction $R_{n\ell}(j)$, and H is a tridiagonal matrix with elements given by

$$H_{ij} = \begin{cases} \frac{\hbar^2}{m^*(\Delta r)^2} + \frac{\ell(\ell+1)}{m^*\left(r_j.\Delta r\right)^2} + V_{\text{WS}}(j), & \text{if } j = i \\ \frac{\hbar^2}{2m^* r_j(\Delta r)} - \frac{\hbar^2}{2m^*(\Delta r)^2}, & \text{if } j = i-1 \\ -\frac{\hbar^2}{2m^* r(\Delta r)} - \frac{\hbar^2}{2m^*(\Delta r)^2}, & \text{if } j = i+1 \\ 0, & \text{otherwise} \end{cases}. \tag{4}$$

In our study, we assume that the radial wavefunction at the external boundary point $(N+1)$ is zero. The dimension of matrix H is $(N \times N)$, and in all of our calculations, we set $N = 1200$ with the boundary condition $R_{n\updownarrow}(r = R_{\text{ext}}) = 0$.

Optical absorption in the QD occurs when an electron in its initial level E_i is excited to a final energy E_f after absorption of a photon with energy $\hbar\omega = \left(E_f - E_i\right)$. According to Fermi's golden rule, the OAC can be written as [45]

$$\alpha(\hbar\omega) = \frac{16\pi^2 \delta_{\text{FS}} P_{if}}{n_r V_{\text{con}}} \hbar\omega \left|M_{if}\right|^2 \delta(E_f - E_i - \hbar\omega), \tag{5}$$

where P_{if}, δ_{FS}, and V_{con} represent the electron population difference, the fine structure, and the confinement volume, respectively. n_r represents the refractive index of the GaAs semiconductor, and $\left|M_{if}\right|$ denotes the DME of the transition. Furthermore, the $\Delta\ell = \pm 1$ selection rule satisfied by the quantum number ℓ is taken into consideration.

In the present paper, we address only the transition between the $1s$ and $1p$ states. Furthermore, the δ-function in the previous equation is substituted with a Lorentzian profile:

$$\delta\left(E_f - E_i - \hbar\omega\right) = \frac{\hbar\Gamma}{\pi\left[\left(E_f - E_i - \hbar\omega\right)^2 + \left(\hbar\Gamma\right)^2\right]}, \tag{6}$$

where $\hbar\omega$ is the energy of the incident photon, and $\hbar\Gamma$ is the width at half height of the Lorentzian function. In the next section, and for simplicity of notation, we consider the initial state $(i = 1)$ to be $1s$ and the final state $(f = 2)$ to be the $1p$ state, so the term $\left|M_{if}\right|^2$

in Equation (3) is simply designated as $|M_{12}|^2$. In our study, the electromagnetic radiation is polarized along the z-axis, and $|M_{12}|^2$ is given by the following expression [50–52]:

$$|M_{12}|^2 = \frac{1}{3}\left|\int_0^\infty R_{1s}(r)r^3R_{1p}(r)dr\right|^2, \tag{7}$$

where the $\frac{1}{3}$ pre-factor arises from integration of the spherical harmonics. In addition to the optical absorption, we have evaluated the impurity binding energy of the neutral donor, defined as $E_b = E_{n,l}^{z=0} - E_{n,l}^{z=1}$, where $E_{n,l}^{z=0}$ and $E_{n,l}^{z=1}$ denote the energy levels for QDs without and with the impurity, respectively.

3. Results and Discussion

Atomic units $(\hbar = e = m_0 = 1)$ are used throughout the rest of this work, which defines the Rydberg energy ($1R_y \cong 5.6$ meV) and Bohr radius ($1a_B \cong 100$ Å). In addition, V_0 is set at 0.228 eV, which corresponds to the band offset between GaAs and $Al_xGa_{(1-x)}As$ with x = 0.3. Additional physical parameters used in our simulation are $\hbar\Gamma = 3$ meV, $m^* = 0.067m_0$, and $\varepsilon = 13.11\varepsilon_0$. The radius of the QD is fixed at $R = 25$ nm.

Figure 3a–d displays the probability densities of the 1s and 1p states with the confining potential in the absence of the hydrogenic impurity (i.e., $Z = 0$) for four values of the structural parameter $(\gamma = 5,\ 10,\ 15,\text{ and } 20\text{ nm})$ with $R_0 = R/2$. Increasing γ also increases the amplitudes of the probability densities of the 1s and 1p states and widens the spatial extent of the wavefunctions. For instance, when $\gamma = 5$ nm, the 1s and 1p densities decay to zero at $r = 15$ and 20 nm, respectively; however, when $\gamma = 20$ nm, both densities decrease to zero at $r = 24$ nm. This behavior is due to the slope of the Woods–Saxon potential decreasing with increasing γ (see Figure 2a–d). The spread in $V_{\text{ws}}(r)$, especially near its top, enhances the amplitudes of the densities and enlarges their geometrical distribution along the r axis. This, in turn, modifies the energy levels and DMEs between the 1s and 1p wavefunctions since their overlap is now modified. Figure 4a–d plots these densities with an on-center hydrogenic impurity. In this case, there are two confining contributions. The first one is due to the geometrical behavior of the $V_{\text{ws}}(r)$ potential due to the increase in the parameter γ, and the second one arises from the electrostatic attraction between the hydrogenic impurity and the electron in different states. This is reflected in the decrease in the amplitudes in the 1s and 1p probabilities. Note that the amplitude for the 1s density is less sensitive than that of 1p for $\gamma = 15$ and 20 nm. For these values, the impact of geometrical confinement becomes negligible compared to that of the electrostatic attraction, and no additional changes are observed for $\gamma > 20$ nm.

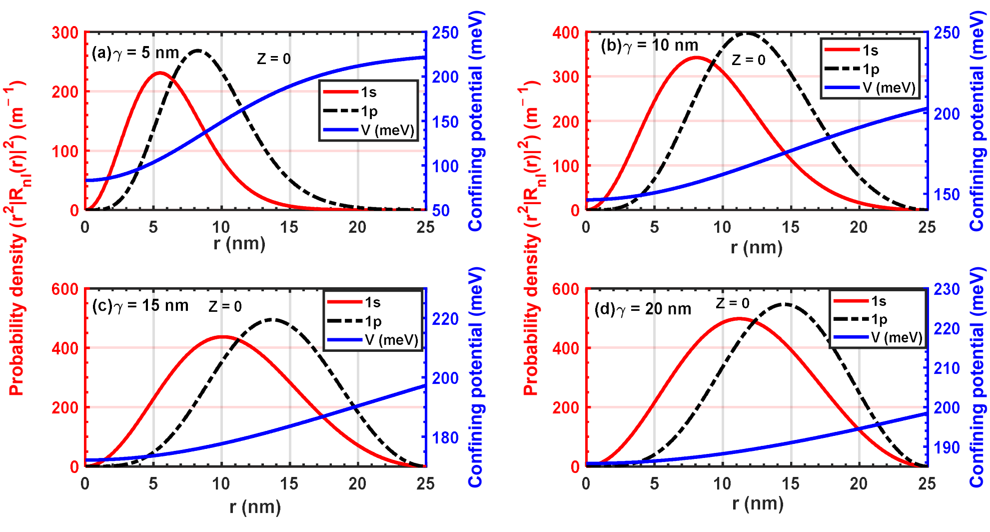

Figure 3. Confining potential and probability densities of the ground and first excited state for different values of γ: (**a**) $\gamma = 5$ nm; (**b**) $\gamma = 10$ nm; (**c**) $\gamma = 15$ nm; (**d**) $\gamma = 20$ nm. All results do not include the impurity $(Z = 0)$. $R_0 = R/2$, $V_0 = 0.228$ eV, and $R_{\text{ext}} = 2R$.

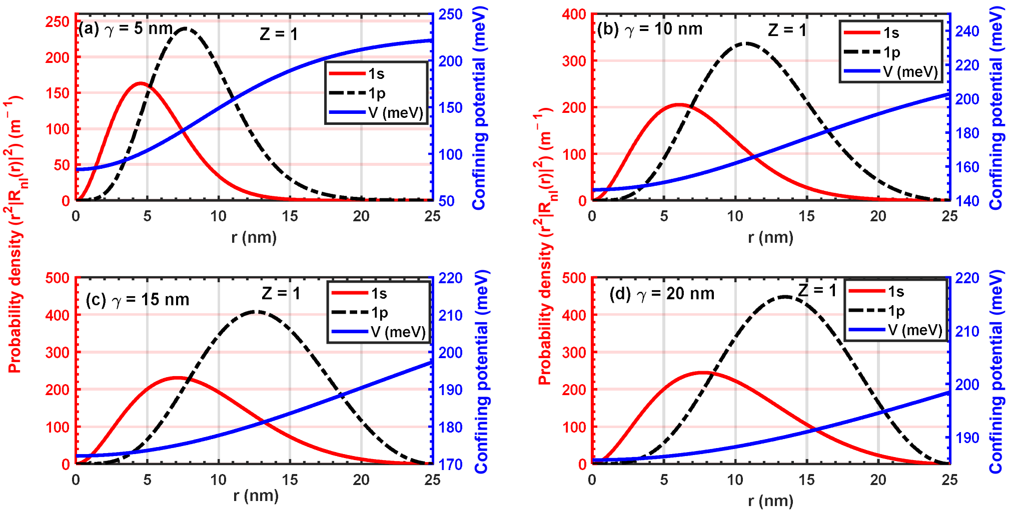

Figure 4. Confining potential and probability densities of the ground and first excited state for different values of γ: (**a**) $\gamma = 5$ nm; (**b**) $\gamma = 10$ nm; (**c**) $\gamma = 15$ nm; and (**d**) $\gamma = 20$ nm. All results include the impurity $(Z = 1)$. $R_0 = R/2$, $V_0 = 0.228$ eV, and $R_{ext} = 2R$.

Figure 5 plots the energy levels E_{1p} and E_{1s}, which increase with γ. At low values of γ, the energy levels are well separated from each other; however, for higher values of γ, their separation is considerably reduced. The decrease in the energy difference between E_{1p} and E_{1s}, with and without the presence of hydrogenic impurity, is responsible for the red shift of the OAC, which we discuss later. Furthermore, for all values of γ, the energy levels in the presence of the hydrogenic impurity are less than those without the hydrogenic impurity. This is due to the attraction between the electron and the impurity, which causes the electron to be near the impurity at the center of the QD.

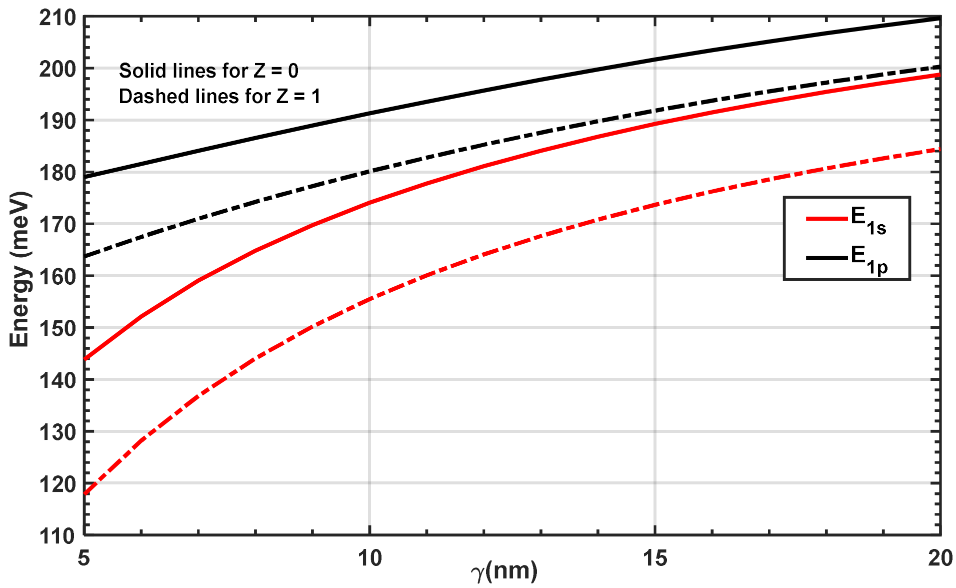

Figure 5. Variation of E_{1s} and E_{1p} for different values of γ with (Z = 1) and without (Z = 0) impurities. $R_0 = R/2$, $V_0 = 0.228$ eV, and $R_{ext} = 2R$.

From Equation (5), the OAC is proportional to $|M_{12}|^2$, which controls the amplitude of the OAC and explains the overlap between the 1s and 1p wavefunctions. Figure 6 plots its variation with the energy separation $(E_{1p} - E_{1s})$ as a function of γ. For $\gamma = 5$ nm, the values of $|M_{12}|^2$ with $(Z = 1)$ and without impurity $(Z = 0)$ are similar. However, when γ is increased, $|M_{12}|^2$ increases and takes higher values for $Z = 0$ than for $Z = 1$. This result is due to the change in the overlap between the 1*s* and 1*p* wavefunctions. In addition, Figure 5 shows that the energy separation $(E_{1p} - E_{1s})$ decreases for both cases (with and without impurity), resulting in a red shift in the OAC.

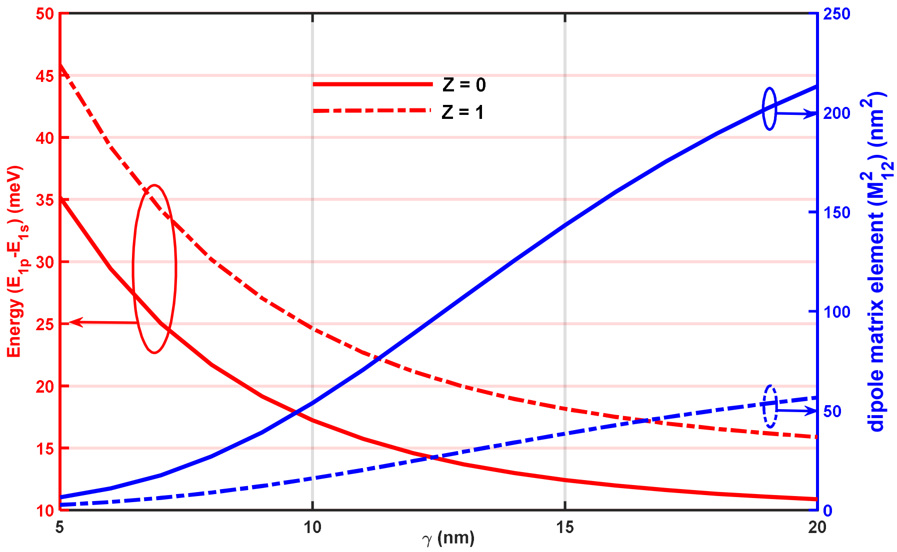

Figure 6. Variation of the energy separation $(E_{1p} - E_{1s})$ and dipole matrix element $|M_{12}|^2$ as a function of the parameter γ for $Z = 0$ (solid line) and $Z = 1$ (dashed line). $R_0 = R/2$, $V_0 = 0.228$ eV, and $R_{\text{ext}} = 2R$.

Figure 7 plots the OAC as a function of photon energy for $\gamma = 5,\ 10,$ and 20 nm. We report results for two cases: with $(Z = 1)$ and without $(Z = 0)$ the hydrogenic impurity. The OAC amplitudes move towards lower energies (red shift) with increasing γ. This variation is in accordance with the variation of $(E_{1p} - E_{1s})$, previously shown in Figure 5. In addition, we note that the OAC amplitudes in the presence of the hydrogenic impurity are always smaller than those without the hydrogenic impurity. This is due to the difference in the DME with and without the presence of the impurity, as shown in Figure 5.

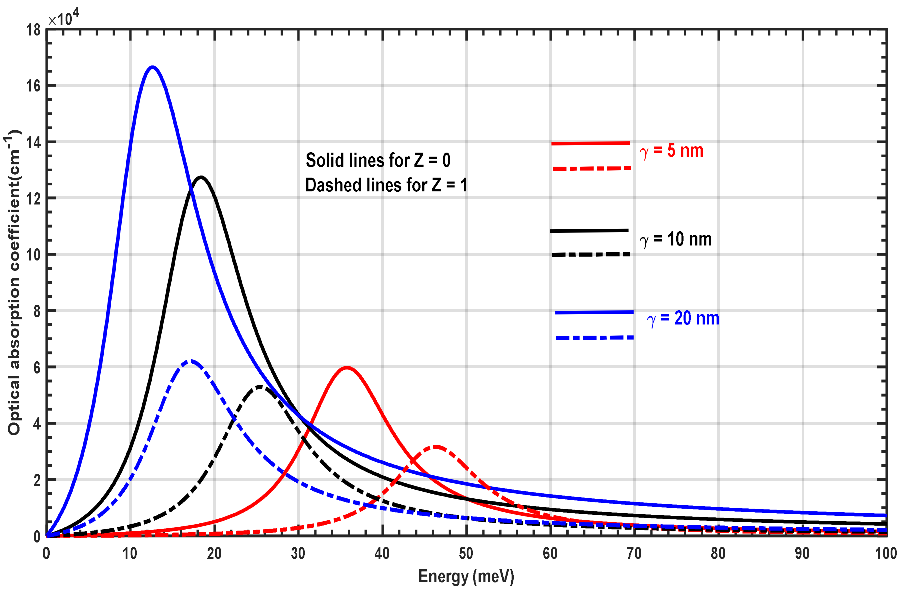

Figure 7. OAC as a function of incident photon energy for different γ values with (Z = 1) and without (Z = 0) impurities. $R_0 = R/2$, $V_0 = 0.228$ eV, and $R_{\text{ext}} = 2R$.

Figure 8 plots the binding energies of the 1*s* and 1*p* states as a function of γ. Both states gradually decrease with γ. For lower values, they decrease rapidly; however, for higher values ($\gamma > 15$ nm), the binding energies show a small variation. This behavior in binding energy for the 1s and 1p states is explained by the strong attraction near the center of the QD; however, for higher values of r, this attraction is reduced compared to the geometrical confinement, and consequently, the binding energy remains constant for all higher values of r.

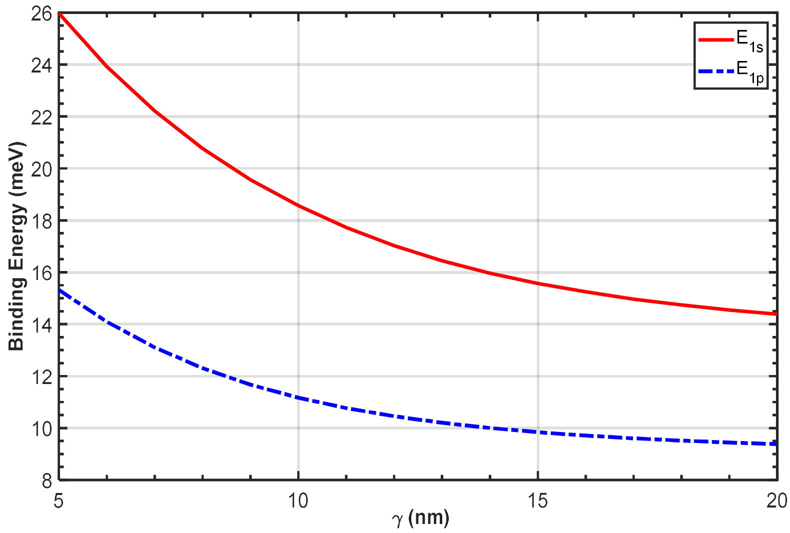

Figure 8. Binding energy for 1s and 1p states as a function of γ. $R_0 = R/2$, $V_0 = 0.228$ eV, and $R_{ext} = 2R$.

We now turn our attention to the effect of R_0. Figure 9a–d plots the probability densities of the lowest electronic states 1s and 1p with the confining potential in the absence of the hydrogenic impurity (i.e., $Z = 0$) for $R_0 = 7, 12, 17,$ and 22 nm, with $\gamma = 10$ nm. Increasing R_0 enlarges the potential and minimizes its values at the center and surface of the quantum dot. Consequently, the two probability densities maintain the same spread; however, their amplitudes increase with R_0. The amplitude of the 1p density is more sensitive than that of 1s when R_0 increases. The influence of the hydrogenic impurity on these densities is shown in Figure 10a–d. The densities have the same spread along the radius of the quantum dot, but their amplitudes are reduced due to the electrostatic attraction introduced by the hydrogenic impurity. To evaluate the effect of the on-center impurity on the OAC, Figure 10 plots its variation as a function of the incident energy for three values of R_0. The OAC peak moves towards higher energy (blue shift) when R_0 increases from 8 to 18 nm. Subsequently, it moves in the direction of low energies, exhibiting a red shift. This double behavior can be interpreted via the variation in the energy separation between the 1s and 1p energy levels.

Figure 11 plots the variation of the 1s and 1p energy levels as a function of R_0, which shows a gradual decrease for the two cases (with and without impurity). This decrease is due to the enlargement of the confining potential with R_0 as shown in Figures 9 and 10. However, the slope of this decrease is slightly different. Figure 12 plots the energy separation $E_{1p} - E_{1s}$ as a function of the parameter R_0, which shows that this separation increases up to $R_0 = 16$ nm but subsequently decreases. This behavior confirms the red and blue shift shown in the OAC variation in Figure 13. In addition, Figure 12 shows the variation of the dipole matrix element $|M_{12}|^2$ as a function of R_0. This physical quantity decreases up to $R_0 = 16$ nm and then subsequently increases. This arises from the variation of the overlap between the R_{1p} and R_{1s} wave functions, which agree with the OAC trends shown in Figure 12. For $R_0 < 16$ nm, the OAC amplitude diminishes; however, for $R_0 > 16$ nm, the amplitude subsequently increases.

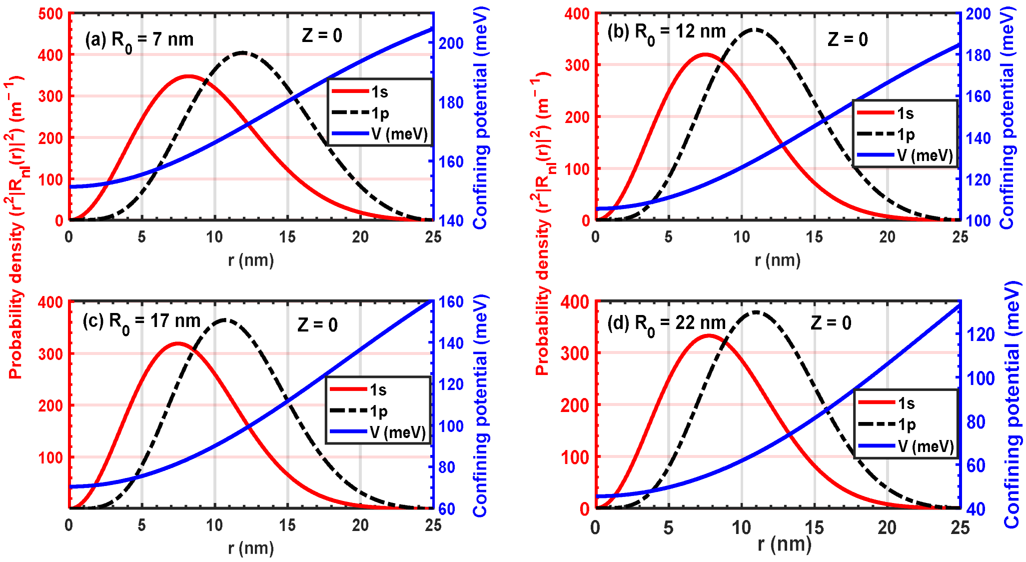

Figure 9. Confining potential and probability densities of the ground and first excited states for different values of R_0: (**a**) $R_0 = 7$ nm; (**b**) $R_0 = 12$ nm; (**c**) $R_0 = 17$ nm; and (**d**) $R_0 = 22$ nm. All results do not include the impurity ($Z = 0$). $\gamma = 10$ nm, $V_0 = 0.228$ eV, and $R = 25$ nm.

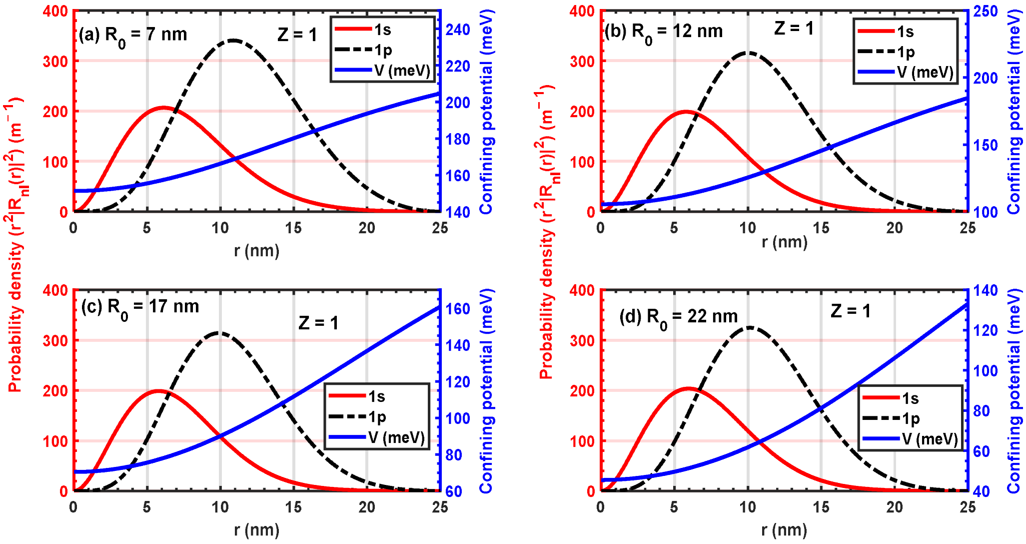

Figure 10. Confining potential and probability densities of the ground and first excited states for different values of R_0: (**a**) $R_0 = 7$ nm; (**b**) $R_0 = 12$ nm; (**c**) $R_0 = 17$ nm; and (**d**) $R_0 = 22$ nm. All results include the impurity ($Z = 1$). $\gamma = 10$ nm, $V_0 = 0.228$ eV, and $R = 25$ nm.

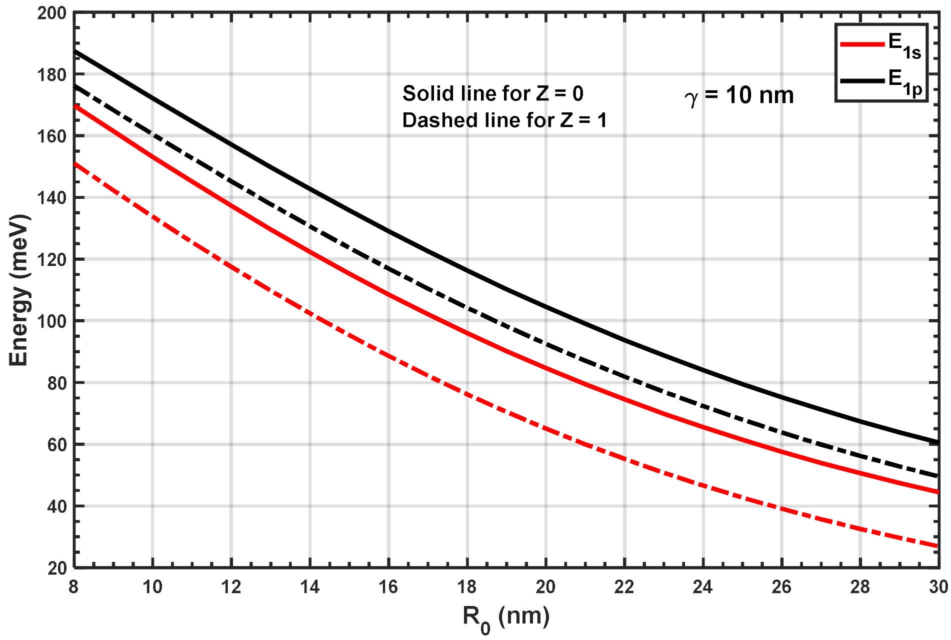

Figure 11. Variation of energy levels E_{1s} and E_{1p} for different values of R_0, with (Z = 1) and without (Z = 0) impurities. $V_0 = 0.228$ eV and $R = 25$ nm.

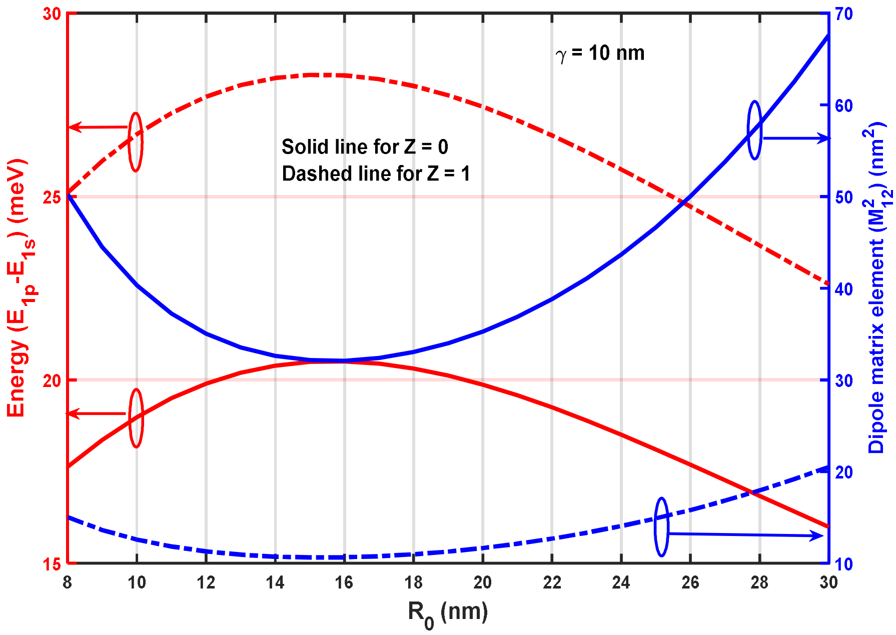

Figure 12. Variation of $E_{1p} - E_{1s}$ and $|M_{12}|^2$ with (dashed curve) and without (solid curve) the on-center impurity as a function of R_0. $V_0 = 0.228$ eV and $R = 25$ nm.

Finally, Figure 14 displays the binding energy as a function of R_0. The binding energy increases up to $R_0 = 16$ nm and subsequently diminishes gradually. Consequently, this critical value of R_0 can play an important role in shifting the OAC from red to blue as well as controlling the variation of the binding energy toward high or low values.

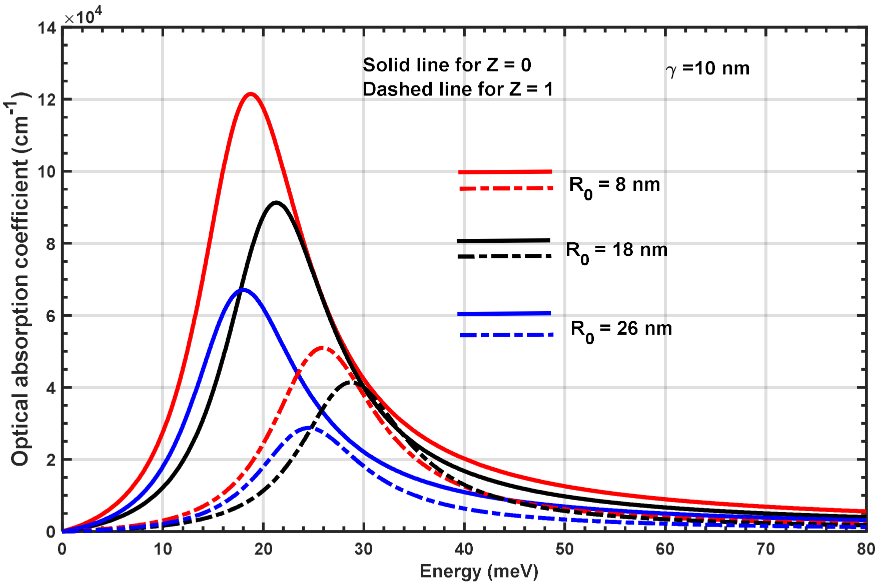

Figure 13. OAC as a function of incident photon energy for different values of R_0. Results are with (Z = 1) and without (Z = 0) impurities. $V_0 = 0.228$ eV and $R = 25$ nm.

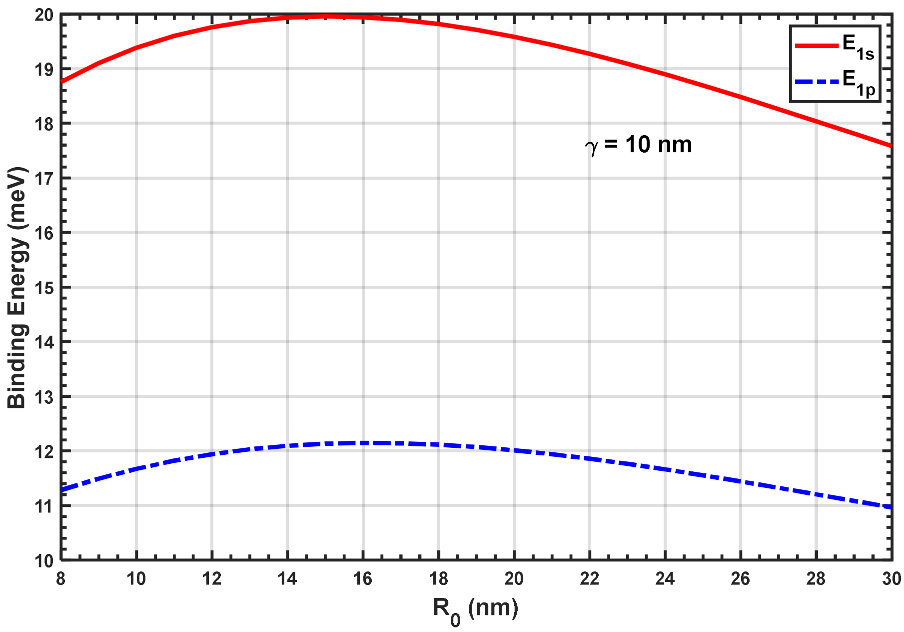

Figure 14. Binding energy for the $1s$ and $1p$ states as a function of R_0. $\gamma = 10$ nm, $V_0 = 0.228$ eV, and $R = 25$ nm.

4. Conclusions

In summary, we have presented the first study of the optical and electronic properties of a GaAs spherical QD with a Woods–Saxon potential in the presence of a hydrogenic impurity. By solving the radial part of the Schrödinger equation using the finite difference method, we obtain energy levels of $1s$ and $1p$ states and their probability densities. These quantities allow us to calculate dipole matrix elements, energy separations, OACs, and binding energies as a function of the parameters R_0 and γ. Our results indicate that increasing γ leads to a red shift of the OAC; however, an increase in R_0 initially gives rise to a blue shift and, subsequently, a red shift. We also demonstrated that the variation of the OAC amplitude is determined via the dipole matrix element, which effectively captures the overlap between R_{1p} and R_{1s}. Moreover, our findings indicate that the insertion of a hydrogenic impurity at the center of the QD considerably decreases the energy levels due to the strong attraction between the free electrons and the hydrogenic impurity. Our numerical calculations provide mechanistic insight into the electronic transport and optical properties of spherical QDs.

Author Contributions: H.D. and W.B. were responsible for the analytical and numerical calculations; H.E. was responsible for formal analysis and writing of the manuscript; F.U. and B.M.W. were responsible for the formal analysis and writing of the manuscript. All authors have read and agreed to the published version of the manuscript.

Funding: H.D., W.B. and H.E. acknowledge the Deputyship for Research and Innovation, Ministry of Education in Saudi Arabia for funding this research work through project number IFP22UQU4331235DSR206. B.M.W. acknowledges support from the UC Riverside Committee on Research grant.

Data Availability Statement: Not applicable.

Conflicts of Interest: The authors declare no conflict of interest.

References

1. Dakhlaoui, H.; Belhadj, W.; Musa, M.O.; Ungan, F. Binding energy, electronic states, and optical absorption in a staircase-like spherical quantum dot with hydrogenic impurity. *Eur. Phys. J. Plus* **2023**, *138*, 519. [CrossRef]
2. Durante, F.; Alves, P.; Karunasiri, G.; Hanson, N.; Byloos, M.; Liu, H.C.; Bezinger, A.; Buchanan, M. NIR, MWIR and LWIR quantum well infrared photodetector using interband and intersubband transitions. *Infrared Phys. Technol.* **2007**, *50*, 182.
3. Imamura, K.; Sugiyama, Y.; Nakata, Y.; Muto, S.; Yokoyama, N. New optical memory structure using self-assembled InAs quantum dots. *Jpn. J. Appl. Phys.* **1995**, *34*, L1445. [CrossRef]
4. Fickenscher, M.; Shi, T.; Jackson, H.E.; Smith, L.M.; Yarrison-Rice, J.M.; Zheng, C.; Miller, P.; Etheridge, J.; Wong, B.M.; Gao, Q.; et al. Optical, structural, and numerical investigations of GaAs/AlGaAs core–multishell nanowire quantum well tubes. *Nano Lett.* **2013**, *13*, 1016–1022. [CrossRef]
5. Marent, A.; Nowozin, T.; Geller, M.; Bimberg, D. The QD-Flash: A quantum dot-based memory device. *Semicond. Sci. Technol.* **2011**, *26*, 014026. [CrossRef]
6. Bonato, L.; Arikan, I.F.; Desplanque, L.; Coinon, C.; Wallart, X.; Wang, Y.; Ruterana, P.; Bimberg, D. Hole localization energy of 1.18 eV in GaSb quantum dots embedded in GaP. *Phys. Status Solidi B* **2016**, *253*, 1869. [CrossRef]
7. Abramkin, D.S.; Atuchin, V.V. Novel InGaSb/AlP Quantum dots for non-volatile memories. *Nanomaterials* **2022**, *12*, 3794. [CrossRef]
8. Abramkin, D.S.; Petrushkov, M.O.; Bogomolov, D.B.; Emelyanov, E.A.; Yesin, M.Y.; Vasev, A.V.; Bloshkin, A.A.; Koptev, E.S.; Putyato, M.A.; Atuchin, V.V.; et al. Structural properties and energy spectrum of novel GaSb/AlP self-assembled quantum dots. *Nanomaterials* **2023**, *13*, 910. [CrossRef]
9. AL-Naghmaisha, A.; Dakhlaoui, H.; Ghrib, T.; Wong, B.M. Effects of magnetic, electric, and intense laser fields on the optical properties of AlGaAs/GaAs quantum wells for terahertz photodetectors. *Phys. B Condens. Matter.* **2022**, *635*, 413838. [CrossRef]
10. Almansour, S.; Dakhlaoui, H.; Algrafy, E. The effect of hydrostatic pressure, temperature and magnetic field on the nonlinear optical properties of asymmetrical Gaussian potential quantum wells. *Chin. Phys. Lett.* **2016**, *33*, 027301.
11. Turkoglu, A.; Dakhlaoui, H.; Mora-Ramos, M.E.; Ungan, F. Optical properties of a quantum well with Razavy confinement potential: Role of applied external field. *Phys. E* **2021**, *134*, 114919. [CrossRef]
12. Dakhlaoui, H.; Altuntas, I.; Mora-Ramos, M.E.; Ungan, F. Numerical simulation of linear and nonlinear optical properties in heterostructure based on triple Gaussian quantum wells: Effects of applied external fields and structural parameters. *Eur. Phys. J. Plus* **2021**, *136*, 894. [CrossRef]
13. Dakhlaoui, H.; Ungan, F.; Martínez-Orozco, J.C.; Mora-Ramos, M.E. Theoretical investigation of linear and nonlinear optical properties in an heterostructure based on triple parabolic barriers: Effects of external fields. *Phys. B* **2021**, *607*, 412782. [CrossRef]
14. Dakhlaoui, H.; Belhadj, W.; Durmuslar, A.S.; Ungan, F.; Abdelkader, A. Numerical study of optical absorption coefficients in Manning-like AlGaAs/GaAs double quantum wells: Effects of doped impurities. *Phys. E Low Dimens. Syst. Nanostruct.* **2023**, *147*, 115623. [CrossRef]
15. Dakhlaoui, H.; Belhadj, W.; Musa, M.O.; Ungan, F. Electronic states and optical characteristics of GaAs Spherical quantum dot based on Konwent-like confining potential: Role of the hydrogenic impurity and structure parameters. *Optik* **2023**, *277*, 170684. [CrossRef]
16. Yoffe, A.D. Semiconductor quantum dots and related systems: Electronic, optical, luminescence and related properties of low dimensional systems. *Adv. Phys.* **2001**, *50*, 1. [CrossRef]
17. Nirmal, M.; Brus, L. Luminescence Photophysics in semiconductor nanocrystals. *Acc. Chem. Res.* **1999**, *32*, 407. [CrossRef]
18. Sargent, E.H. Colloidal quantum dot solar cells. *Nat. Photon.* **2012**, *6*, 133. [CrossRef]
19. Bouzaiene, L.; Alamri, H.; Sfaxi, L.; Maaref, H. Simultaneous effects of hydrostatic pressure, temperature and electric field on optical absorption in InAs/GaAs lens shape quantum dot. *J. Alloys Compd.* **2016**, *655*, 172. [CrossRef]

20. Ben Mahrsia, R.; Choubani, M.; Bouzaiene, L.; Maaref, H. Second-harmonic generation in vertically coupled InAs/GaAs quantum dots with a Gaussian potential distribution: Combined effects of electromagnetic fields, pressure, and temperature. *Electron. Mater.* **2015**, *44*, 2792. [CrossRef]
21. Al-Marhaby, F.A.; Al-Ghamdi, M.S. Experimental investigation of stripe cavity length effect on threshold current density for InP/AlGaInP QD laser diode. *Opt. Mater.* **2022**, *127*, 112191. [CrossRef]
22. Chuang, C.H.M.; Brown, P.R.; Bulović, V.; Bawendi, M.G. Improved performance and stability in quantum dot solar cells through band alignment engineering. *Nat. Mater.* **2014**, *13*, 796. [CrossRef]
23. De Franceschi, S.; Kouwenhoven, L.; Schönenberger, C.; Wernsdorfer, W. Hybrid superconductor–quantum dot devices. *Nat. Nanotechnol.* **2010**, *5*, 703. [CrossRef] [PubMed]
24. Gao, X.; Yang, L.; Petros, J.A.; Marshall, F.F.; Simons, J.W.; Nie, S. In vivo molecular and cellular imaging with quantum dots. *Cur. Opin. Biotechnol.* **2005**, *16*, 63. [CrossRef]
25. Medintz, I.L.; Clapp, A.R.; Mattoussi, H.; Goldman, E.R.; Fisher, B.; Mauro, J.M. Self-assembled nanoscale biosensors based on quantum dot FRET donors. *Nat. Mater.* **2003**, *2*, 630. [CrossRef] [PubMed]
26. Loss, D.; DiVincenzo, D.P. Quantum computation with quantum dots. *Phys. Rev. A* **1998**, *57*, 120. [CrossRef]
27. Al-Sheikhi, A.; Al-Abedi, N.A.A. The luminescent emission and quantum optical efficiency of $Cd_{1-x}Sr_xSe$ QDs developed via ions exchange approach for multicolor-lasing materials and LED applications. *Optik* **2021**, *227*, 166035. [CrossRef]
28. Al-Ahmadi, N.A. The anti-crossing and dipping spectral behavior of coupled nanocrystal system under the influence of the magnetic field. *Results Phys.* **2021**, *22*, 103835.
29. Galiautdinov, A. Ground state of an exciton in a three-dimensional parabolic quantum dot: Convergent perturbative calculation. *Phys. Lett. A* **2018**, *382*, 72. [CrossRef]
30. Vahdani, M.R.K.; Rezaei, G. Intersubband optical absorption coefficients and refractive index changes in a parabolic cylinder quantum dot. *Phys. Lett. A* **2010**, *374*, 637. [CrossRef]
31. Khordad, R. Use of modified Gaussian potential to study an exciton in a spherical quantum dot. *Superlattices Microstruct.* **2013**, *54*, 7. [CrossRef]
32. Sakiroglu, S.; Kasapoglu, S.; Restrepo, R.L.; Duque, C.A.; Sökmen, I. Intense laser field-induced nonlinear optical properties of Morse quantum well. *Phys. Stat. Solidi B* **2017**, *254*, 1600457. [CrossRef]
33. Prasad, V.; Silotia, P. Effect of laser radiation on optical properties of disk-shaped quantum dot in magnetic fields. *Phys. Lett. A* **2011**, *375*, 3910. [CrossRef]
34. Lee, S.W.; Hirakava, K.; Shimada, Y. Bound-to-continuum intersubband photoconductivity of self-assembled InAs quantum dots in modulation-doped heterostructures. *Appl. Phys. Lett.* **1999**, *75*, 1428. [CrossRef]
35. Klimov, V.I.; McBranch, D.W.; Leatherdale, C.A.; Bawendi, M.G. Electron and hole relaxation pathways in semiconductor quantum dots. *Phys. Rev. B* **1999**, *60*, 13740. [CrossRef]
36. Mackowski, S.; Kyrychenko, F.; Karczewski, G.; Kossut, J.; Heiss, W.; Prechtl, G. Thermal carrier escape and capture in CdTe quantum dots. *Phys. Stat. Solidi B* **2001**, *224*, 465. [CrossRef]
37. Sauvage, S.; Boucaud, P.; Brunhes, T.; Immer, V.; Finkman, E.; Gerard, J.M. Midinfrared absorption and photocurrent spectroscopy of InAs/GaAs self-assembled quantum dot. *Appl. Phys. Lett.* **2001**, *78*, 2327. [CrossRef]
38. Schrey, F.F.; Rebohle, L.; Muller, T.; Strasser, G.; Unterrainer, K.; Nguyen, D.P.; Regnault, N.; Ferreira, R.; Bastard, G. Intraband transitions in quantum dot–superlattice heterostructures. *Phys. Rev. B* **2005**, *72*, 155310. [CrossRef]
39. Bahar, M.K.; Baser, P. Nonlinear optical characteristics of thermodynamic effects-and electric field-triggered Mathieu quantum dot. *Micro Nanostruct.* **2022**, *170*, 207371. [CrossRef]
40. Batra, K.; Prasad, V. Spherical quantum dot in Kratzer confining potential: Study of linear and nonlinear optical absorption coefficients and refractive index changes. *Eur. Phys. J. B* **2018**, *91*, 298. [CrossRef]
41. Buczko, R.; Bassani, F. Bound and resonant electron states in quantum dots: The optical spectrum. *Phys. Rev. B* **1996**, *54*, 2667. [CrossRef]
42. Narvaez, G.A.; Zunger, A. Calculation of conduction-to-conduction and valence-to-valence transitions between bound states in (In, Ga)As/GaAs quantum dots. *Phys. Rev. B* **2007**, *75*, 085306. [CrossRef]
43. Stoleru, V.G.; Towe, E. Oscillator strength for intraband transitions in (In, Ga)As/GaAs. *Appl. Phys. Lett.* **2003**, *83*, 5026. [CrossRef]
44. Yilmaz, S.; Safak, H. Oscillator strengths for the intersubband transitions in a CdS–SiO_2 quantum dot with hydrogenic impurity. *Phys. E* **2007**, *36*, 40. [CrossRef]
45. Costa, L.S.D.; Prudente, F.V.; Acioli, P.H.; Neto, J.S.; Vianna, J.D.M. A study of confined quantum systems using the Woods-Saxon potential. *J. Phys. B At. Mol. Opt. Phys.* **1999**, *32*, 2461. [CrossRef]
46. Fakkahi, A.; Sali, A.; Jaouane, M.; Arraoui, R.; Ed-Dahmouny, A. Study of photoionization cross section and binding energy of shallow donor impurity in multilayered spherical quantum dot. *Phys. E* **2022**, *143*, 115351. [CrossRef]
47. Sali, A.; Satori, H.; Fliyou, M.; Loumrhari, H. The photoionization cross-section of impurities in quantum dots. *Phys. Status Solidi* **2002**, *232*, 209. [CrossRef]
48. Holovatsky, V.; Chubrei, M.; Yurchenko, O. Impurity photoionization cross-section and intersubband optical absorption coefficient in multilayer spherical quantum dots. *Phys. Chem. Solid. State* **2021**, *22*, 630. [CrossRef]
49. Arraoui, R.; Sali, A.; Ed-Dahmouny, A.; Jaouane, M.; Fakkahi, A. Polaronic mass and non-parabolicity effects on the photoionization cross section of an impurity in a double quantum dot. *Superlattice Microst.* **2021**, *159*, 107049. [CrossRef]

50. Sahin, M.; Koksal, K. The linear optical properties of a multi-shell spherical quantum dot of a parabolic confinement for cases with and without a hydrogenic impurity. *Semicond. Sci. Technol.* **2012**, *27*, 125011. [CrossRef]
51. Ed-Dahmouny, A.; Arraoui, R.; Jaouane, M.; Fakkahi, A.; Sali, A.; Es-Sbai, N.; El-Bakkari, K.; Zeiri, N.; Duque, C.A. The influence of the electric and magnetic fields on donor impurity electronic states and optical absorption coefficients in a core/shell GaAs/$Al_{0.33}Ga_{0.67}As$ ellipsoidal quantum dot. *Eur. Phys. J. Plus* **2023**, *138*, 774. [CrossRef]
52. Ed-Dahmouny, A.; Zeiri, N.; Arraoui, R.; Es-Sbai, N.; Jaouane, M.; Fakkahi, A.; Sali, A.; El-Bakkari, K.; Duque, C.A. The third-order nonlinear optical susceptibility in an ellipsoidal core-shell quantum dot embedded in various dielectric surrounding matrices. *Phys. E* **2023**, *153*, 115784. [CrossRef]